



Full length article



Lightweight, ultrastrong and high thermal-stable eutectic high-entropy alloys for elevated-temperature applications

Mingliang Wang^a, Yiping Lu^{a,*}, Jinggang Lan^{b,*}, Tongmin Wang^a, Chuan Zhang^c,
Zhiqiang Cao^a, Tingju Li^a, Peter K. Liaw^{d,*}

^a Key Laboratory of Solidification Control and Digital Preparation Technology (Liaoning Province), School of Materials Science and Engineering, Dalian University of Technology, Dalian 116024, PR China

^b Department of Chemistry, University of Zurich, Winterthurerstrasse 190, Zurich 8057, Switzerland

^c CompuTherm LLC, Middleton, WI 53562, USA

^d Department of Materials Science and Engineering, The University of Tennessee, Knoxville, TN 37996, USA

ARTICLE INFO

Keywords:

Eutectic high-entropy alloy
High-temperature strength
Low density
Thermal stability
Nanoprecipitates

ABSTRACT

Eutectic high-entropy alloys (EHEAs) that combine the advantages of HEAs and eutectic alloys are promising candidates for high-temperature applications. However, currently developed EHEAs still exhibit high densities and low high-temperature strengths, which limit their usage. Here we propose a strategy to design lightweight, strong, and high thermal-stable EHEAs by introducing an extremely stable Heusler-type ordered phase (L₂₁ phase) containing a high-content of low-density elements and constructing a low lattice misfit eutectic-phase interface, which can lead to generate ultrafine and stable lamellar structures and high-density of coherent nanoprecipitates. As a manifestation of this strategy, a novel bulk Al₁₇Ni₃₄Ti₁₇V₃₂ EHEA was designed to consist of L₂₁ and body-centered-cubic (BCC) phases (interlamellar spacing ~ 320 nm) with a lattice misfit only 2.4%. This alloy has one of the lowest densities (~ 6.2 g/cm³) among all EHEAs reported previously and exhibits much higher high-temperature hardness and specific yield strengths than most reported refractory HEAs (RHEAs), lightweight HEAs (LWHEAs), EHEAs, and conventional superalloys. This work paves the way to develop light EHEAs with excellent high-temperature properties.

1. Introduction

Fossil energy and aerospace are currently working toward longer endurance, lower energy consumption, and lower carbon emissions [1, 2]. Traditional Ni-based superalloys have served these key industries for decades, but they have gradually reached their service temperature limits, as well as been inherently expensive and high density. [3,4]. Novel Fe-based superalloys with significant cost advantage and relatively low densities have been developed to attempt to replace or partially substitute for Ni-based superalloys [5,6], but they still exhibit some drawbacks, such as the low high-temperature strengths and insufficient lightweight. Therefore, new high-temperature structural materials are urgently required that should be lighter, stronger, and more thermally stable to obtain further efficiency gains and environmental friendliness in the next generation of aero engines and gas-turbine engines.

Eutectic high-entropy alloys (EHEAs) [7,8] as a subclass of HEAs [9,

10], which can combine the advantages of HEAs and eutectic alloys [11], are superior candidates for high-temperature applications. Up to now, there are dozens of different EHEA systems having been developed, and they can be roughly classified into two categories based on the structures of eutectic phases. The first category is composed of face-centered-cubic (FCC) and B2 phases, such as AlCoCrFeNi_{2.1} [12–15], Al₁₉Fe₂₀Co₂₀Ni₄₁ [16,17], CrFeNi_{2.2}Al_{0.8} [18], Ni₃₀Co₃₀Cr₁₀Fe₁₀Al₁₈W₂ [19], Al_{19.3}Co₁₅Cr₁₅Ni_{50.7} [20], Fe_{28.2}Ni_{18.8}Mn_{32.9}Al_{14.1}Cr₆ [21], Al₁₇Co_{28.6}Cr_{14.3}Fe_{14.3}Ni_{25.8} [22], and Al_{17.4}Co_{21.7}Cr_{21.7}Ni_{39.2} [23]. This type of EHEAs usually have an excellent strength-ductility combination at room temperature, but their high-temperature mechanical properties are poor due to the low strength of the FCC phase and the poor creep resistance of the B2 phase at elevated temperatures. The second one consisted of the FCC phase and uncommon intermetallic compounds (IMCs), such as CoCrFeNiNb_{0.45} [24], CoCrFeNiMnPd_x [25], V₁₀Cr₁₅Mn₅Co₁₀Ni₂₅Fe_{25.3}Nb_{9.7} [26], CoFeNi_{1.4}VMo [27], Co₂Mo_{0.8}Ni₂VW_{0.8} [28], Zr_{0.6}CoCrFeNi_{2.0} [29],

* Corresponding authors.

E-mail addresses: luyiping@dlut.edu.cn (Y. Lu), jinggang.lan@epfl.ch (J. Lan), pliaw@utk.edu (P.K. Liaw).

<https://doi.org/10.1016/j.actamat.2023.118806>

Received 21 July 2022; Received in revised form 16 February 2023; Accepted 21 February 2023

Available online 24 February 2023

1359-6454/© 2023 Acta Materialia Inc. Published by Elsevier Ltd. All rights reserved.

Hf_{0.55}CoCrFeNi_{2.0} [29], CoCrFeNiTa_{0.4} [30], and CrFeNi_{1.85}V_{0.64}Ta_{0.36} [31]. This class of EHEAs generally possess high strengths because of their strengthening effects of hard IMCs that have multiple types with various complex crystal structures. Nevertheless, the most stable polype remains unclear, and phase transition may occur as the temperature and/or applied stress change in these IMCs [32]. In addition, their crystal structures are quite different from that of the FCC phase, which indicates that it is difficult to form low misfit coherent/semi-coherent eutectic phase interface with a high interfacial bonding strength. These above and other issues will cause considerable difficulty to control the microstructures and properties of the EHEAs. In particular, the current reported EHEAs exhibit relatively high densities, which are nearly all larger than 7.0 g/cm³ (see Table S1). Therefore, the current EHEAs cannot yet satisfy the requirement for high-temperature applications.

Our very recent preliminary work firstly discovered potential body-centered-cubic (BCC) – Heusler (L2₁) dual-phase EHEA with similar crystal structures and low lattice misfit (~ 1.90%) in an Al–Cr–Ti–Ni system, which has uniform and ultrafine lamellar structures (interlamellar spacing of ~ 400 nm) and exhibits low density (~ 6.4 g/cm³), superior high-temperature mechanical properties, and outstanding thermal stability [33].

Motivated by the previous work [33], we propose a systematic design strategy for the development of lightweight, ultrastrong, and high thermal-stable EHEAs by introducing an extremely stable Heusler-type ordered phase containing high contents of low-density elements and constructing a low lattice misfit eutectic-phase interface (see the Supplementary material for more details on the design strategy). To establish the validity of this strategy, a novel Al–Ni–Ti–V system EHEA (i.e., Al₁₇Ni₃₄Ti₁₇V₃₂) that is composed of Ni–Al–Ti-rich L2₁ and V-rich BCC phases was designed. This EHEA has one of the lowest densities (~ 6.2 g/cm³) among the current reported EHEAs and ultrafine lamellar structures (interlamellar spacing of ~ 320 nm) and exhibits outstanding thermal stability and much superior high-temperature mechanical properties, compared to the most reported refractory HEAs (RHEAs), lightweight HEAs (LWHEAs), EHEAs, and conventional Ni-/Ti-based alloys. The inherent thermal stable and strengthening mechanisms were revealed by experimental studies and theoretical analyzes, including transmission electron microscopy (TEM) and three-dimensional (3D) atom probe tomography (3DAPT) characterizations, high-temperature hardness and compression tests, ab-initio molecular dynamics (AIMD) simulations, density functional theory (DFT) calculations, and CALculated PHase Diagram (CALPHAD) predictions. The present work provides valuable insight into the development of high-performance lightweight EHEAs useful for applications at elevated temperatures.

2. Materials and methods

2.1. Alloy fabrication

Bulk EHEA ingots with the predetermined compositions of Al₁₇Ni₃₄Ti₁₇V₃₂ were prepared from > 99.9 wt% (wt%) pure metals using arc melting. The ingots were melted five times to ensure chemical homogeneity. The densities of the bulk ingots were measured, using the Archimedes drainage method by a ME204E balance with a precision of 0.0001 g. In general, the apparent softening will occur in conventional Ni-based superalloys when the temperature is above 650 °C, such as Inconel 718, GH4169, and NC19FeNb, due to the unfavorable phase transformation (e.g. formation of detrimental phases, etc.) and the coarsening of γ' and γ'' strengthening phases [34–38]. This indicates the instability of phase structure in such Ni-based superalloys. In order to verify that the present EHEA has the excellent phase structure and size stability at temperatures beyond 650 °C, and also to confirm that this EHEA has the potential to replace Ni-based superalloys at higher temperatures, a typical heat treatment of annealing at 800 °C for 30 h, in an argon atmosphere, was selected.

2.2. Microstructure characterization

Both the as-cast and annealed samples were polished using standard metallographic procedure, and their microstructural morphologies were examined via an electron probe microanalyzer (EPMA) (JXA-8530F PLUS). The phase constituents of the alloys were identified by the X-ray diffraction (XRD) (Empyrean, Holland) with Cu K α radiation between a scanning 2θ range of 20 and 100° and at a scanning rate of 4° min⁻¹. The XRD patterns were analyzed using the Rietveld structural refinement approach as implemented in the General Structure Analysis System (GSAS) package [39]. In the Rietveld analysis, the refined parameters included scale factor, background, shift lattice constants, profile half-width parameters, isotropic thermal parameters, strain anisotropy factor, occupancy, atomic functional positions, bond lengths and bond angles. The Rietveld refinement was processed following the Rietveld refinement guidelines formulated by the International Union of Crystallography Commission on powder diffraction [40]. Firstly, the Rietveld refinement was based on the V-rich BCC phase and Ni₂AlTi-type L2₁ phase. The space group of IM-3M and FM-3M were indicated in PDF card 22–1058 and 54–0386, respectively. The background was corrected using a Chebyshev polynomial of the first kind. The diffraction peak profiles were better fitted by the Thompson–Cox–Hastings pseudo-Voigt function and by the asymmetry function described by Finger et al. [41]. The strain anisotropy was corrected by the phenomenological model described by Stephens to obtain more accurate lattice parameters [42]. If the R_{wp} factor that was obtained after the Rietveld refinement of the XRD data was not more than 10%, the reliabilities of the refinements were close to the ideal results.

The samples for electron-backscattered diffraction (EBSD) studies were electro-polished in a solution of 10% perchloric acid and 90% ethanol at 30 V for 5 s at -25 °C, and the EBSD tests were conducted on an FEI Quanta 650F scanning electron microscope equipped with an automatic orientation acquisition system (Oxford Instruments-HKL Channel 5). The thermal behavior of the EHEA was analyzed by differential scanning calorimeter (DSC) (Netzsch STA 449 F3) from 50 to 1600 °C with a heating/cooling rate of 10 °C/min. in an argon atmosphere. TEM characterizations were conducted on an FEI Tecnai G2 F20 S-TWIN operating at 200 kV. Two methods were used to fabricate the TEM foil samples. The as-cast and annealed samples were prepared by an FEI Helios Nanolab 600i dual-beam focused ion beam (FIB) instrument using a Ga-ion beam for milling. The deformed samples with a plastic strain of ~ 10% at 800 °C were prepared by twin-jet polishing on the 3 mm-diameter disks, using an electrolyte consisting of 95% (volume percent) ethanol and 5% perchloric acid in a volume fraction at a temperature of -40 °C and an applied voltage of 30 V. The 3DAPT sharp-tip samples were prepared by a FEI Nova 200 dual-beam FIB instrument. The APT measurements were performed, using a local electrode atom probe (LEAP 4000 XHR, CAMECA Instruments, USA). The APT data were reconstructed and analyzed, using the IVAS 3.8 software provided by CAMECA Instruments. A double-tilt heating holder with a tantalum furnace (Model 652, Gatan, Inc., Pleasanton, CA, USA) was used for the *in-situ* TEM observation. The TEM thin foil was employed for continuous heating from RT to 600 °C, then to 800 °C, and at last to 1000 °C using the smart mode. This sample was conducted for holding for 10 min. at each elevated temperature, and the BF TEM images and selected-area electron diffraction (SAED) patterns were obtained at the corresponding temperature after holding for 10 min.

2.3. Mechanical tests

The alloy samples with dimensions of 10 mm × 10 mm × 2 mm were ground and then mechanically polished by using standard metallographic procedure for hot hardness tests. The hot hardness tests were conducted both on the as-cast and annealed samples at RT, 400, 600, 800, and 900 °C, employing a high-temperature Vickers hardness tester (HTV-PHS30, England). The alloys were cut into rod-type samples with

size of 8 mm in diameter and 12 mm in length for compression tests. The sample surfaces were polished with sandpaper to remove the wire-electrode cutting trace. Uniaxial compression tests were conducted both on as-cast and annealed samples at RT, 600, 700, 800, 900, 1000, and 1100 °C, using a thermo-mechanical simulator (Gleeble3800) operating at a strain rate of 10^{-3} s^{-1} . Each test was repeated three times to ensure the consistent data, and the average values (e.g., the stress-strain curves, yield strengths, and plastic strains) are presented.

2.4. CALPHAD calculations

The CALPHAD calculations were conducted, using the Pandat 2021.1 software and its PanHEA2021 database, developed by CompuTherm LLC [43]. In the present work, the eutectic point between the Heusler (L_{21}) and BCC phases was predicted by establishing the pseudo-binary Ni_2AlTi (L_{21}) – V (BCC) phase diagram via thermodynamic calculations. The phase transformation at the eutectic point composition was predicted during solidification to be used for phase thermal stability.

2.5. AIMD & DFT simulations

All electronic structure simulations are employed, using the CP2K package [44]. Perdew-Burke-Ernzerhof (PBE) functional [45] with the Grimme D3 correction [46] was used to describe the system. Kohn-Sham DFT has been used as the electronic-structure method in the framework of the Gaussian and plane waves method [47,48]. The Goedecker-Teter-Hutter (GTH) pseudopotentials [49,50], DZVP-MOLOPT-GTH basis sets [47], were utilized to describe the molecules. A plane-wave energy cut-off of 500 Ry has been employed.

The AIMD simulations are carried out, using the NVT ensemble at 3000 K using Canonical sampling through velocity rescaling [51] with the time step of 2 fs. The simulation was conducted in a three-dimensional periodic boundary box of $11.68 \times 11.68 \times 11.68 \text{ \AA}^3$ with a cubic supercell of 128 atoms for the Al-Ni-Ti-V system. We equilibrate the system for about 2 ps and a time length of 8 ps was used to analyze and calculate radial distribution function. The partial PDF [$g_{ab}(r)$] can be calculated, employing the following equation [4]:

$$g_{ab}(r) = \frac{V}{N_a N_b} \frac{1}{4\pi r^2} \sum_{i=1}^{N_a} \sum_{j=1}^{N_b} \delta(|r_{ij}| - r) \quad (1)$$

where V is the volume of the supercell, N_a and N_b are the numbers of elements, a and b , $|r_{ij}|$ is the distance between elements, a and b , and the bracket, $\langle \rangle$, represents the time average of different configurations.

The diffusion constants of each element in the liquid state can also be predicted by AIMD simulation through plotting the mean square displacement (MSD) versus time, using the following equation [4]:

$$D_i = \lim_{t \rightarrow \infty} \frac{|R_i(t) - R_i(0)|^2}{6t} \quad (2)$$

where D_i is the self-diffusion constant of species, i , and $R_i(t)$ and $R_i(0)$ denote the atomic position of species, i , at time, t , and $t = 0$, respectively. The angular brackets represent an average over all the same species.

The total-energy calculations at zero temperature were carried out on selected ternary and quaternary L_{21} phase to analyze the trend of the alloying elemental substitution. All the structures were fully relaxed with respect to the volume and the atomic coordinates. The configuration that resulted in the lowest energy was used for data analysis. The energies of formation (E_f) of the various virtual compositions in ternary and quaternary systems via DFT calculations utilizing the following equation:

$$E_f = \frac{1}{a + b + c + d} [E(\text{Ni}_a\text{Al}_b\text{Ti}_c\text{V}_d) - aE(\text{Ni}) - bE(\text{Al}) - cE(\text{Ti}) - dE(\text{V})] \quad (3)$$

where the a , b , c , and d are the number of atoms for Ni, Al, Ti, and V. E ($\text{Ni}_a\text{Al}_b\text{Ti}_c\text{V}_d$) is the total energy of alloy, and $E(M)$ ($M = \text{Ni, Al, Ti, V}$) is the energy of pure element in its stable structure.

3. Results

3.1. Phase and microstructures of the $\text{Al}_{17}\text{Ni}_{34}\text{Ti}_{17}\text{V}_{32}$ EHEA

Systematic phase and microstructural characterizations of the as-cast and annealed $\text{Al}_{17}\text{Ni}_{34}\text{Ti}_{17}\text{V}_{32}$ alloy were conducted not only to obtain the detailed microstructural data, but also to evaluate the thermal stability of this alloy (Figs. 1 - 4, S4-S7).

In the as-cast state, the $\text{Al}_{17}\text{Ni}_{34}\text{Ti}_{17}\text{V}_{32}$ alloy exhibits a uniform and ultrafine lamellar microstructure (Fig. 1(a)). The XRD pattern in Fig. 1(c) demonstrates that this alloy is composed of ordered L_{21} (exhibiting the low-angle superlattice diffraction peaks at 2θ values of 26.1° and 30.3°) and disordered BCC phases. The EBSD phase map (the inset in Fig. 1(c)) indicates that the coarse and fine lamellae correspond to L_{21} and BCC structures, respectively. The DSC results (Fig. S4) reveal that only one melting event is present both in the heating and cooling curves, which substantiates the eutectic composition in the $\text{Al}_{17}\text{Ni}_{34}\text{Ti}_{17}\text{V}_{32}$ alloy. The statistical lamellar width distribution based on numerous backscattered electron (BSE) images, and EBSD maps reveals that the average lamellar widths for the L_{21} ($\lambda_{L_{21}}$) and BCC (λ_{BCC}) phases are 199.4 nm and 123.1 nm, respectively (Fig. 1(d)). Thus, the eutectic interlamellar spacing ($\lambda_e = \lambda_{L_{21}} + \lambda_{\text{BCC}}$) of the as-cast $\text{Al}_{17}\text{Ni}_{34}\text{Ti}_{17}\text{V}_{32}$ alloy is determined to be 322.5 nm. After annealing at 800 °C for 30 h (Fig. 1(b)), the ultrafine eutectic lamellar morphology ($\lambda_e = 332$ nm, see Fig. 1(e)) and dual-phase L_{21} and BCC structures are sustained (Fig. 1(c)), which indicates the excellent phase structure and size stability of the EHEA up to 800 °C at the present annealing time scale. In addition, the measured density of the $\text{Al}_{17}\text{Ni}_{34}\text{Ti}_{17}\text{V}_{32}$ EHEA is 6.178 g/cm^3 , close to its theoretical density of 6.209 g/cm^3 , which heretofore represents one of the lowest densities among all EHEAs reported previously (see Table S1).

The TEM analysis was conducted to further identify the detailed information within the eutectic phases (Fig. 2). The SAED patterns along two different zone axes ($[001]$ and $[011]$) further reveal that the eutectic phases are composed of L_{21} and BCC structures (Fig. 2(a) and (b)). Note that some faint superlattice reflections are also present in both $[001]$ and $[011]$ zone axes SAED patterns of the BCC phase (Fig. 2(b)), indicating the possibility of ordering within the BCC phase. The bright-field (BF) TEM image in Fig. 2(c) indicates a high-density of precipitates within the BCC matrix. The high-magnification dark-field (DF) TEM image in Fig. 2(d) obtained from the superlattice spot of $\{111\}$ (the inset of Fig. 2(d)) suggests that the precipitates and BCC matrix exhibit bright and dark contrast, respectively, indicating that the precipitates have the L_{21} -ordered structure, while the BCC matrix has a disordered structure. This is further substantiated by the high-resolution TEM (HRTEM) characterization (Fig. 2(e)) and the corresponding electron-diffraction patterns from the fast Fourier transform (FFT) (insets of Fig. 2(e)) containing both the precipitates and BCC matrix. Additionally, a coherent interface between the L_{21} precipitate and BCC matrix is identified by the HRTEM characterization.

The BF TEM image in Fig. 2(f) indicates that there are also abundant precipitates within the eutectic L_{21} phase. An HRTEM image of the eutectic L_{21} phase is shown in Fig. 2(g), wherein two typical precipitates are embedded within the L_{21} matrix. The electron-diffraction patterns from FFT for precipitates (the upper right inset of Fig. 2(g)) and L_{21} matrix (the upper left inset of Fig. 2(g)) reveal that the precipitates and matrix have the disordered BCC and ordered L_{21} structures, respectively. Furthermore, a magnified HRTEM image presented in the lower right inset of Fig. 2(g) demonstrates that the BCC precipitates have a coherent interface with the L_{21} matrix. An HRTEM image showing the eutectic phase interface of L_{21}/BCC is displayed in Fig. 2(h), wherein the

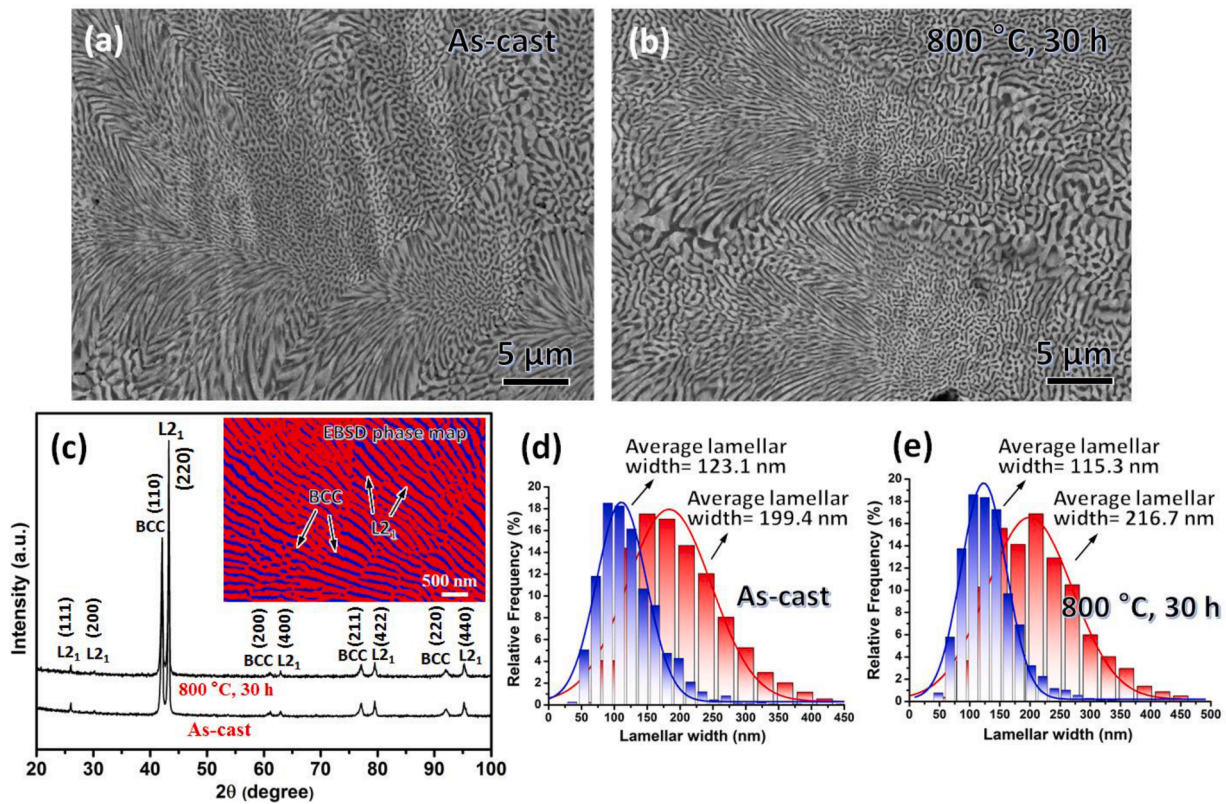


Fig. 1. Phase and microstructural information of the $\text{Al}_{17}\text{Ni}_{34}\text{Ti}_{17}\text{V}_{32}$ alloy. (a–b) Backscattered electron (BSE) images of the as-cast and annealed alloys, respectively. (c) XRD patterns of the as-cast and annealed alloys. Inset shows the EBSD phase map of the as-cast alloy. (d–e) The statistical lamellar width distribution of the as-cast and annealed alloys, respectively.

corresponding electron-diffraction patterns from FFT for both phases are shown as insets. The magnified HRTEM image from the inverse FFT (IFFT) corresponding to the interfacial region of L_{21}/BCC in Fig. 2(i) reveals that a high density of edge dislocations is present at the eutectic phase interface. This feature can also be observed in the BF TEM image in Fig. 2(c), wherein there are abundant misfit dislocations along the eutectic phase interface. Combining the Rietveld refinement results on XRD pattern (Fig. S5) and HRTEM characterization, the lattice parameters for the eutectic BCC phase (a_{BCC}) and L_{21} phase ($a_{\text{L}_{21}}$) are calculated to be 0.3028 and 0.5909 nm. Thus, the lattice misfit (δ) between the eutectic L_{21} and BCC phases is determined to be only 2.4% using Eq. (4) [4]:

$$\delta = \frac{2(a_{\text{L}_{21}} - 2a_{\text{BCC}})}{(a_{\text{L}_{21}} + 2a_{\text{BCC}})} \quad (4)$$

The orientation relationship between the eutectic L_{21} and BCC phases can be identified as $[001]_{\text{L}_{21}} \parallel [001]_{\text{BCC}}$ from the above HRTEM characterization on the eutectic phase interface (Fig. 2(h) and (i)). Consequently, both the lower δ value (2.4%) and HRTEM characterization indicate that a cube-on-cube semi-coherent interface between the eutectic L_{21} and BCC phases has been formed. In our design strategy (see the first part of Supplementary Materials), we have tried to design a new kind of EHEA system containing eutectic Heusler (L_{21}) and BCC phases. The similar crystal structures and low lattice misfit between L_{21} and BCC phases can decrease the nucleation barrier for eutectic phases and nanoprecipitates, and thus refine microstructures and stabilize the eutectic phases and nanoprecipitates with a high number density. Thus it can be seen, the present experimental observations agree well with the model predictions of initial EHEA design.

To further identify the compositions and morphologies of the eutectic phases and nanoprecipitates, a detailed 3DAPT analysis was conducted (Figs. 3 and 4). The 3D-reconstruction-ion maps containing

various elements for the eutectic BCC phase in Fig. 3(a) reveal that a high density of Al-Ni-Ti-rich (L_{21}) precipitates are dispersed within the BCC matrix that is enriched in V. This trend can be observed more clearly from the 22 atomic percent (at%) Ni + 11 at% Al + 11 at% Ti + V-isosurface. Fig. 3(b) shows the 3D-reconstruction-ion maps of a typical L_{21} precipitate, wherein the Al, Ni, and Ti atomic clusters can be clearly observed. One-dimensional compositional profiles across the interface of the BCC matrix/precipitate further suggest that Al, Ni, and Ti are partitioned into the L_{21} precipitate, and V is partitioned into the matrix (Fig. 3(c)). The L_{21} precipitates contain an average composition of 21.91 at% Al, 38.90 at% Ni, 22.39 at% Ti, and 16.80 at% V measured by extracting 2 nm diameter spheres from dozens of precipitates to produce the bulk composition of these spheres, while the BCC matrix has an average composition of 81.02 at% V, 7.11 at% Ni, 3.63 at% Ti, and 8.24 at% Al. The statistical size distribution from numerous TEM images and 3D-reconstruction ion maps reveals that the average diameter for the L_{21} precipitates is 3.11 nm (Fig. 3(d)).

The 3D-reconstruction-ion maps of various elements, including the eutectic L_{21} phase and a small part of the BCC phase, are shown in Fig. 4 (a). Evidently, Al, Ni, and Ti are partitioned into the L_{21} phase, and V is partitioned into the BCC phase, which is further substantiated by the one-dimensional compositional profiles spanning the eutectic phase interface (Fig. 4(b)). Additionally, V-rich (BCC) precipitates that are dispersed inside the L_{21} matrix can be observed from the 9 at% V-isosurface. The 3D-reconstruction-ion maps corresponding to a typical BCC precipitate clearly reveal the presence of V-atomic clusters (Fig. 4(c)). This trend can also be substantiated by the one-dimensional compositional profiles across the L_{21} matrix/BCC precipitate interface presented in Fig. 4(d). Utilizing the same method with the composition measurement of L_{21} precipitates, the BCC precipitates have an average composition of 43.36 at% V, 26.45 at% Ni, 13.10 at% Ti, and 17.09 at% Al, and the L_{21} matrix has an average composition of 25.37 at% Al, 47.03 at%

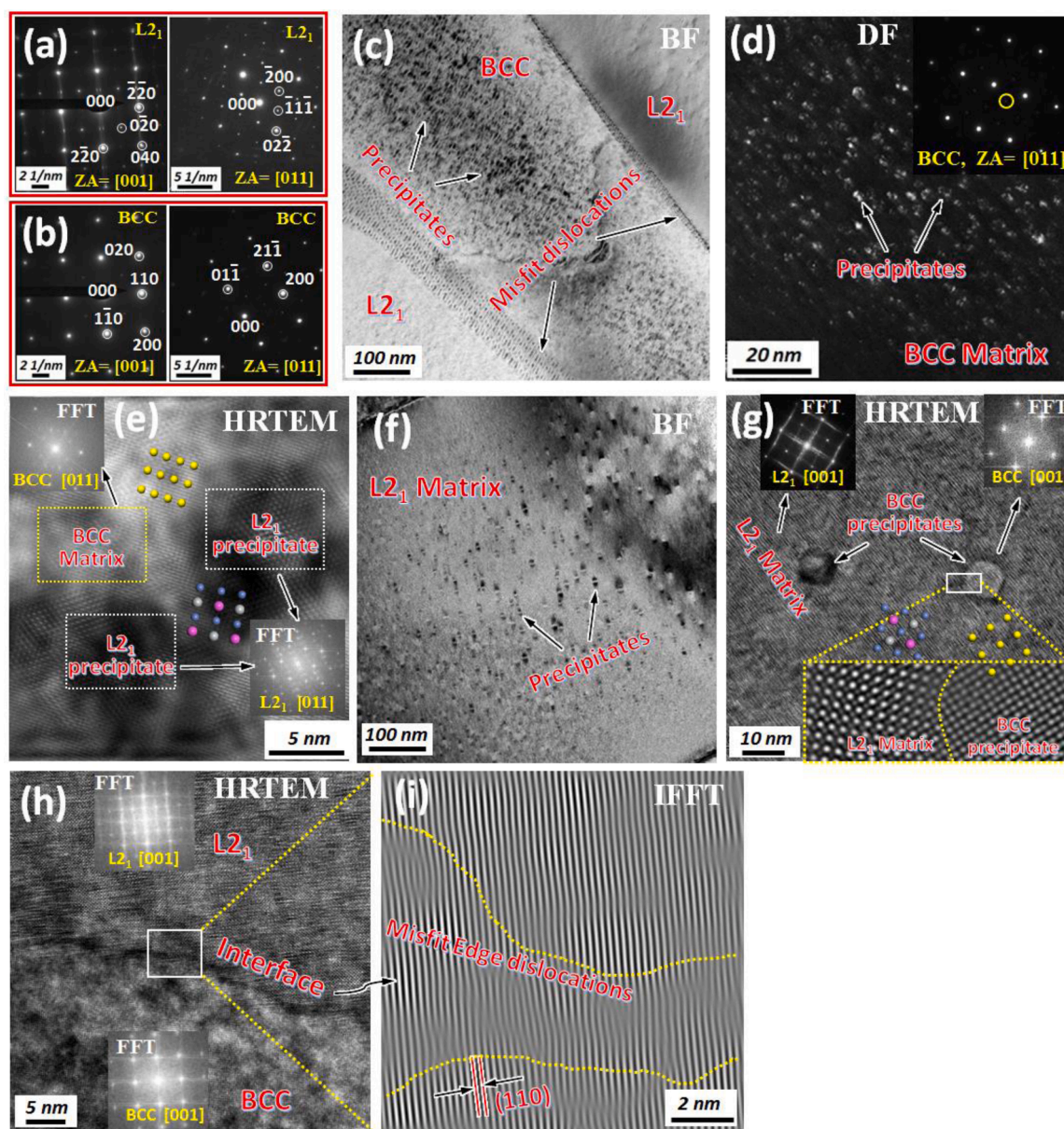


Fig. 2. TEM characterization of the $\text{Al}_{17}\text{Ni}_{34}\text{Ti}_{17}\text{V}_{32}$ alloy. (a–b) SAED patterns along two different zone axes ($[001]$ and $[011]$) for eutectic L_{21} and BCC phases, respectively. (c) BF TEM image of the as-cast alloy, showing a high density of nanoprecipitates within the BCC phase. (d) DF TEM image of the BCC phase for the as-cast alloy obtained from the $\{111\}$ superlattice spot encircled in yellow in the inset of (d). Inset shows the SAED pattern of the $[011]$ zone axis for the BCC phase. (e) HRTEM image of the as-cast alloy, showing the L_{21} precipitates embedded inside the BCC matrix. The upper left inset presents the electron-diffraction pattern (EDP) of the BCC matrix from FFT; the lower right inset shows the EDP of the L_{21} precipitate from FFT. (f) BF TEM image of the as-cast alloy, showing the distribution of precipitates within the eutectic L_{21} phase. (g) HRTEM image exhibiting the BCC precipitates embedded inside the L_{21} matrix. The upper left inset shows the EDP of the L_{21} matrix from FFT; the upper right inset shows the EDP of the BCC precipitate from FFT; the lower right inset presents a magnified HRTEM image for the interface of the BCC precipitate/ L_{21} matrix. (h) HRTEM image of the as-cast alloy, showing the eutectic-phase interface of L_{21} /BCC. The upper and lower insets show the EDPs of the eutectic L_{21} and BCC phases, respectively. (i) A magnified-HRTEM image from the inverse FFT showing the interfacial region in (h).

Ni, 24.82 at% Ti, and 2.78 at% V. The statistical size distribution indicates that the BCC precipitates have an average diameter of 3.59 nm (Fig. 4(e)). Summarizing, the eutectic BCC phase that has a high-level of V (> 80 at%) is a V-rich phase, which contains a high density of Al-Ni-Ti-rich L_{21} precipitates, while the eutectic L_{21} phase that is rich in Al (~ 25 at%), Ti (~ 25 at%), and Ni (~ 47 at%) can be identified as an Ni_2AlTi -type Heusler phase, wherein the V-rich BCC precipitates are present. The formation of nanoprecipitates is a diffusive phase-transformation behavior in HEAs, mainly due to the interaction of multiple elements and the presence of intrinsic coherent interface between the precipitates and matrix [52–54].

In addition, the morphologies of both precipitates after annealing at

800°C for 30 h were characterized by TEM (Figs. S6(a), (b)). The average sizes of the L_{21} and the BCC precipitates were determined to be 9.93 nm (Fig. S6(c)) and 13.40 nm (Fig. S6(d)), respectively. Although both types of precipitates have grown and coarsened after annealing, compared to the as-cast state, they still remain spherical and a smaller size of approximately 10 nm. Furthermore, an *in-situ* TEM study was performed to real-time monitor the structural stability of eutectic phases at elevated temperatures (600, 800, and 1000°C , see Fig. S7). Both the BF TEM images and SAED patterns were obtained at each corresponding temperature after holding for 10 min. Note that the SAED patterns of both eutectic phases remain nearly unchanged from RT to 1000°C , which further substantiates that the present EHEA has an outstanding

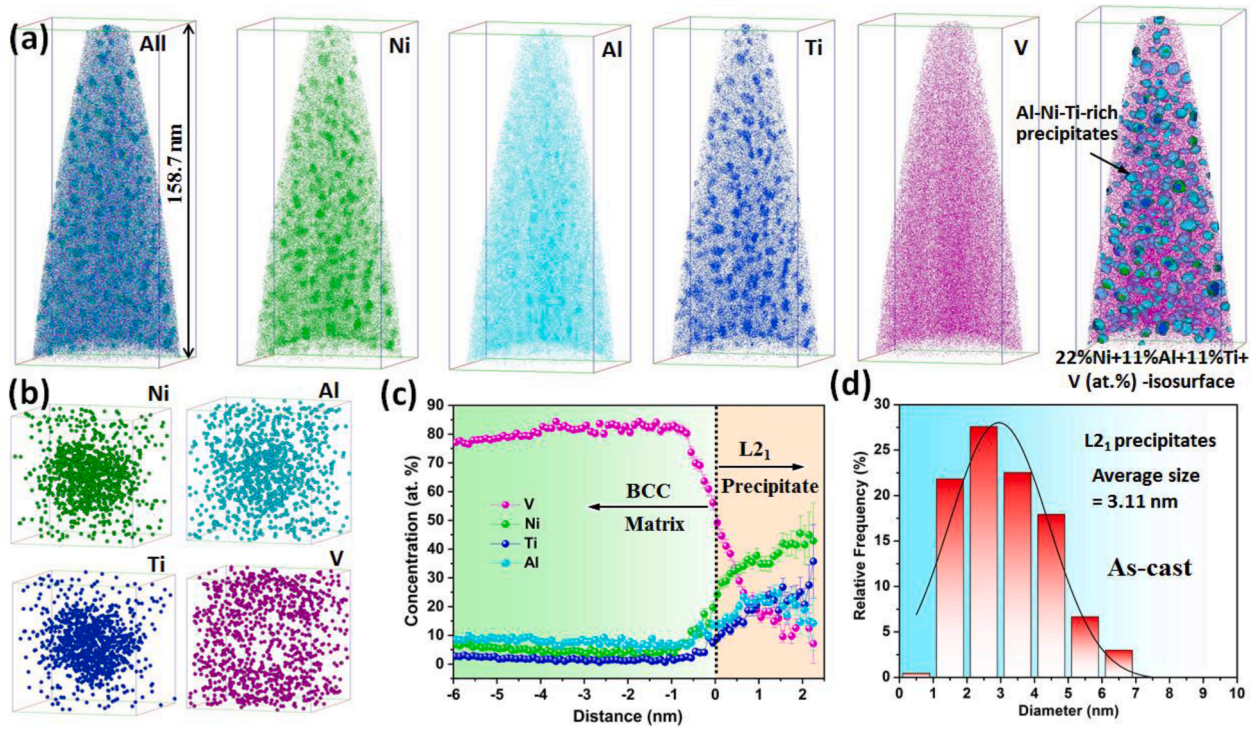


Fig. 3. APT characterization on the eutectic BCC phase. (a) 3D-reconstruction ion maps containing the various elements. (b) 3D-reconstruction of ion maps captured from a L₂₁ precipitate in (a), showing the Al, Ni, and Ti atomic clusters. (c) One-dimensional compositional profiles across the interface of the L₂₁ precipitate/BCC matrix. (d) The statistical size distribution of L₂₁ nanoprecipitates.

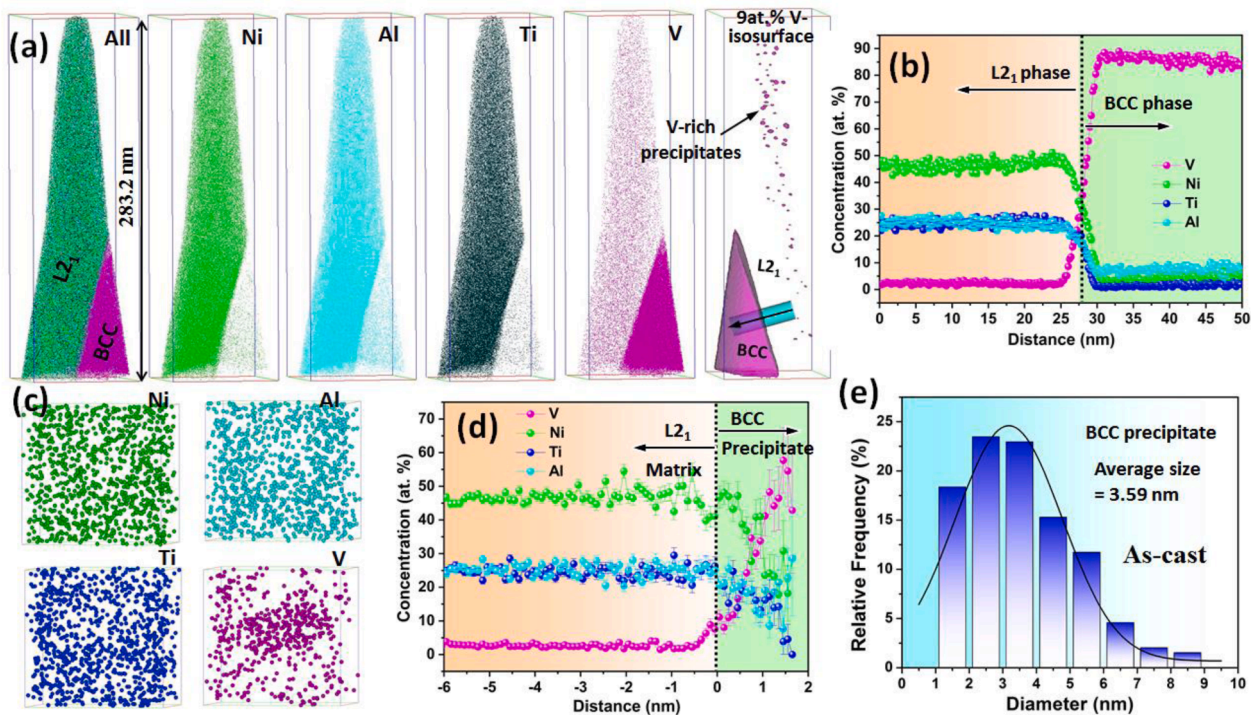


Fig. 4. APT characterization on the eutectic L₂₁ phase. (a) 3D-reconstruction-ion maps of various elements, including the eutectic L₂₁ phase and a small part of the BCC phase. (b) One-dimensional compositional profiles across the eutectic-phase interface of BCC/L₂₁. (c) The 3D-reconstruction of ion maps captured from a BCC nanoprecipitate in (a), showing the V atomic clusters. (d) One-dimensional compositional profiles across the interface of the BCC precipitate/L₂₁ matrix. (e) The statistical-size distribution of BCC nanoprecipitates.

phase structural stability.

3.2. Mechanical properties of the $Al_{17}Ni_{34}Ti_{17}V_{32}$ EHEA at elevated temperatures

To evaluate the high-temperature mechanical properties of the $Al_{17}Ni_{34}Ti_{17}V_{32}$ EHEA, we performed hardness and compression tests on both the as-cast and annealed alloys (800 °C, 30 h) at elevated

Table 1

Hardness (HV_{0.3}) of the $Al_{17}Ni_{34}Ti_{17}V_{32}$ EHEA at elevated temperatures.

	RT	400 °C	600 °C	800 °C	900 °C
As-cast	489 ± 18	478 ± 24	474 ± 19	459 ± 24	446 ± 18
Annealing (800 °C, 30 h)	478 ± 11	470 ± 18	464 ± 17	455 ± 17	440 ± 25

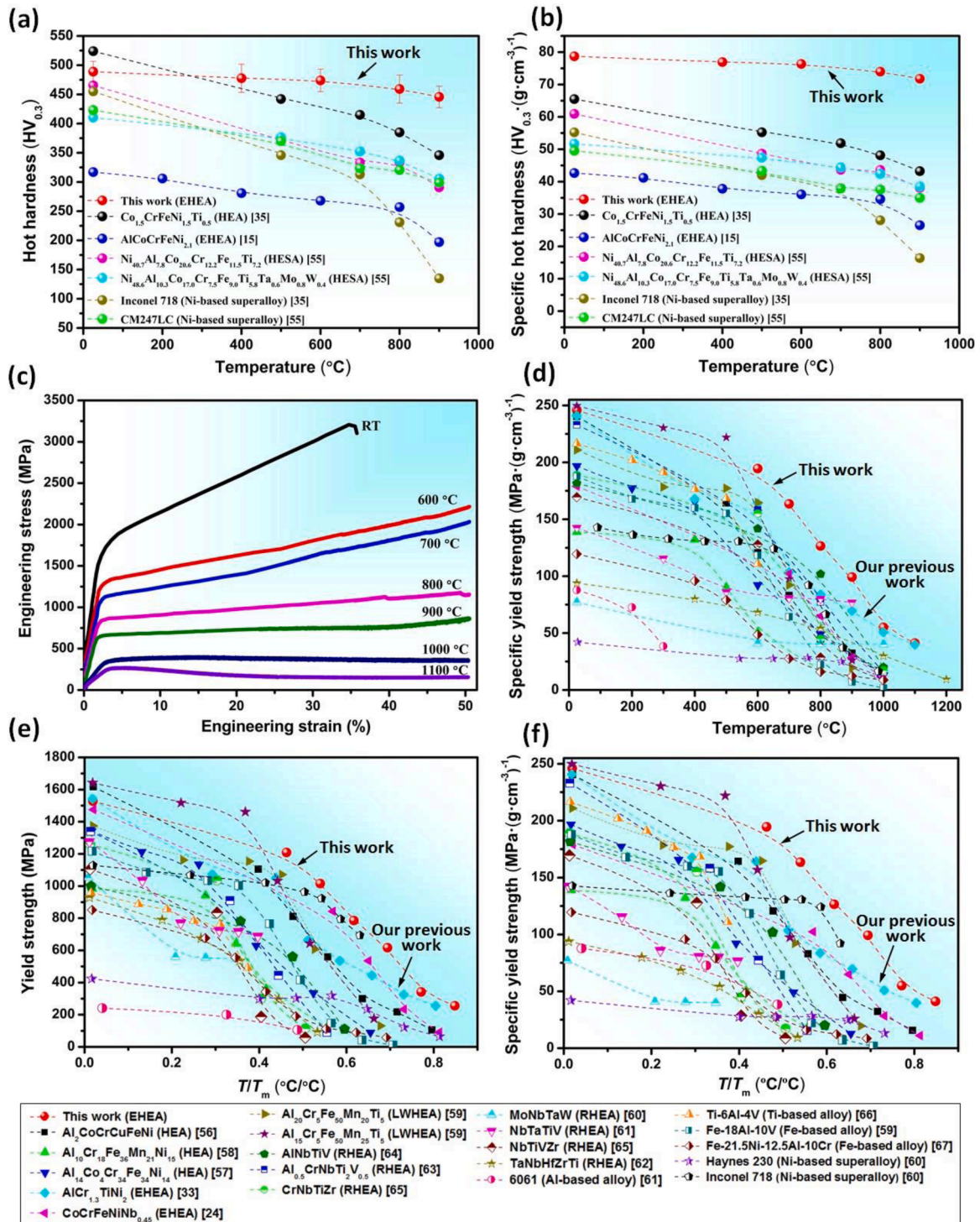


Fig. 5. Mechanical properties of the as-cast $Al_{17}Ni_{34}Ti_{17}V_{32}$ alloy at elevated temperatures. (a-b) Hardness and specific hardness as a function of testing temperature of this alloy in comparison with other representative alloys [15,35,55], respectively. (c) Compressive engineering stress-strain curves at various temperatures. (d) SYS as a function of testing temperature of this alloy in comparison with other representative alloys [24,33,56-67]. (e-f) Yield strength and SYS as a function of homologous temperature (T/T_m) of this alloy in comparison with other representative alloys, respectively.

Table 2
Yield strengths (MPa) of the $\text{Al}_{17}\text{Ni}_{34}\text{Ti}_{17}\text{V}_{32}$ EHEA at elevated temperatures.

	RT	600 °C	700 °C	800 °C	900 °C	1000 °C	1100 °C
As-cast	1527 ± 38	1209 ± 24	1015 ± 22	786 ± 18	616 ± 21	342 ± 13	256 ± 9
Annealing (800 °C, 30 h)	1464 ± 35	1153 ± 28	970 ± 19	746 ± 21	582 ± 17	330 ± 16	237 ± 8

temperatures (Figs. 5, S8 and Tables 1, 2). Note that the tensile tests were also conducted on as-cast samples from room temperature to 1100 °C. However, we failed to obtain any available results from this test due to the intrinsic brittleness of this EHEA system.

The hardness of the as-cast $\text{Al}_{17}\text{Ni}_{34}\text{Ti}_{17}\text{V}_{32}$ EHEA from room temperature to 900 °C was evaluated and compared to other representative alloys (Fig. 5(a) and Table 1) [15,35,55]. Among the surveyed alloys, $\text{Al}_{17}\text{Ni}_{34}\text{Ti}_{17}\text{V}_{32}$ has a higher hardness throughout all temperatures, especially at elevated temperatures, compared to these reported high-entropy superalloys (HESAs), EHEA, and traditional Ni-based superalloys. Although the hardness of the $\text{Al}_{17}\text{Ni}_{34}\text{Ti}_{17}\text{V}_{32}$ EHEA is lower than that of the $\text{Co}_{1.5}\text{CrFeNi}_{1.5}\text{Ti}_{0.5}$ HEA at room temperature, it far exceeds the HEA at elevated temperatures, which suggests that the $\text{Al}_{17}\text{Ni}_{34}\text{Ti}_{17}\text{V}_{32}$ EHEA has a strong resistance of high-temperature softening. Furthermore, the comparison of the specific hot hardness displayed in Fig. 5(b) indicates that the $\text{Al}_{17}\text{Ni}_{34}\text{Ti}_{17}\text{V}_{32}$ EHEA exhibits more obvious advantage due to its lower density and higher hardness, compared to the other representative alloys.

The compression tests were performed from room temperature to 1100 °C to further evaluate the elevated-temperature mechanical properties of the $\text{Al}_{17}\text{Ni}_{34}\text{Ti}_{17}\text{V}_{32}$ EHEA (Figs. 5(c)–(f), S8, Table 2). Although the yield strengths of this alloy gradually decrease with increasing temperature, they still maintain the rather high levels at elevated temperatures, such as 1209 ± 24 MPa at 600 °C, $1,016 \pm 22$ MPa at 700 °C, and 786 ± 18 MPa at 800 °C in the as-cast state (Fig. 5(c) and Table 2). The temperature dependence of the specific yield strength (SYS) of the as-cast EHEA was evaluated and compared to other reported up to twenty alloys (Fig. 5(d)), containing the representative HEAs [56–58], EHEAs [24,33], LWHEAs [59], RHEAs [60–65], and traditional Al-based alloy [61], Ti-based alloy [66], Fe-based alloys [59,67], and Ni-based superalloys [60]. Evidently, the $\text{Al}_{17}\text{Ni}_{34}\text{Ti}_{17}\text{V}_{32}$ EHEA exhibits the highest SYS above 600 °C among the surveyed alloys, far outperforming other representative alloys except our previous reported $\text{AlCr}_{1.3}\text{TiNi}_2$ EHEA [33] that has the comparable SYS values with the present $\text{Al}_{17}\text{Ni}_{34}\text{Ti}_{17}\text{V}_{32}$ alloy both at 1000 and 1100 °C. In addition, the temperature dependence of the yield strength and SYS of these alloys are summarized in Fig. 5(e) and (f) as a function of the homologous temperature, i.e., the ratio of testing temperature/melting temperature (T/T_m), respectively. Among the investigated alloys, the present $\text{Al}_{17}\text{Ni}_{34}\text{Ti}_{17}\text{V}_{32}$ EHEA exhibits both the highest yield strength and SYS when the value of T/T_m is above ~ 0.45 , especially the SYS, suggesting that the $\text{Al}_{17}\text{Ni}_{34}\text{Ti}_{17}\text{V}_{32}$ EHEA has strong high-temperature softening resistance. In general, the softening will occur in an alloy when the temperature is above $0.5\text{--}0.6 T_m$ due to the activation of diffusion-controlled deformation mechanisms [68]. For instance, although the precipitation-strengthened $\text{Al}_{15}\text{Cr}_5\text{Fe}_{50}\text{Mn}_{25}\text{Ti}_5$ LWHEA has both the highest yield strength and SYS from room temperature to 500 °C ($T/T_m \approx 0.37$) (Fig. 5(d)–(f)) among the investigated alloys, it softens rapidly with the further increase of temperature. However, the above trend is not totally supported by the T/T_m dependence of yield strength or SYS for the present $\text{Al}_{17}\text{Ni}_{34}\text{Ti}_{17}\text{V}_{32}$ alloy. The measured melting temperature of the $\text{Al}_{17}\text{Ni}_{34}\text{Ti}_{17}\text{V}_{32}$ EHEA is 1296.85 °C (Fig. S4), which is lower than that of most other representative alloys shown in Fig. 5(d)–(f), especially these RHEAs. Surprisingly, $\text{Al}_{17}\text{Ni}_{34}\text{Ti}_{17}\text{V}_{32}$ has both the highest yield strength and SYS when the value of T/T_m is above ~ 0.45 among these alloys. In addition, both the hardness and SYS of the annealed EHEA exhibit very slight reduction, compared to the as-cast state (Tables 1, 2, and Fig. S8), indicating that an exceptional thermal stability of the present EHEA resulted from the thermally

stable phases and microstructures. Moreover, our previous reported $\text{AlCr}_{1.3}\text{TiNi}_2$ EHEA [33] with L2_1 and BCC structures also exhibits rather high levels in both the yield strength and SYS at elevated temperatures (see Fig. 5(d)–(f)), which indicates that the present design strategy has the validity and universality for developing lightweight, strong, and high thermal-stable EHEAs for elevated-temperature applications.

4. Discussion

4.1. Mechanisms of thermal stability

The phase and microstructural thermal stability, which can greatly impact the mechanical properties at elevated temperatures, is one of the crucial criteria to determine whether a high-temperature structural material can reliably serve for a long time. The above experimental results indicate that the present $\text{Al}_{17}\text{Ni}_{34}\text{Ti}_{17}\text{V}_{32}$ EHEA exhibits an outstanding thermal stability. Herein, the underlying mechanisms of the phase and microstructural thermal stability for this EHEA were discussed, based on experimental analyzes, first-principles studies, including the AIMD and DFT calculations, and CALPHAD prediction.

The aforementioned experimental results revealed that the $\text{Al}_{17}\text{Ni}_{34}\text{Ti}_{17}\text{V}_{32}$ EHEA is composed of the L2_1 phase (containing the L2_1 eutectic phase and L2_1 precipitates) and BCC phase (containing the BCC eutectic phase and BCC precipitates). The L2_1 phase is rich in Ni, Al, and Ti and lean in V, while the BCC phase is enriched in V, and depleted of Ni, Al, and Ti, which is consistent with the model predictions of initial EHEA design (see the first part of Supplementary Materials). Generally, the formation and stability of phases are closely related to their chemical compositions. The chemical distribution in the L2_1 phase indicates that there may be a coupled role of Ni, Ti, and Al related to the formation and stability of the L2_1 phase. The AIMD simulations can reveal the preferred interatomic bonding in the liquid state that has an effect on the phase formation during solidification, and the probability of such bond formation can be determined by the partial pair distribution function (PDF) via the measurement of the intensity of near-neighbor pairs against the distribution of atoms [4,69]. The partial PDFs (Fig. 6(a)) reveal the existence of the preferred first-nearest-neighbor pair correlation of Ni-Al, Ni-Ti, and Ti-Al, which indicates the strong tendency for Ni, Al, and Ti to form short-range ordered structures in the liquid state. By contrast, the Al-Al, Ni-Ni, Ti-Ti, V-Al, V-Ni, V-Ti, and V-V are among those less favorable pairs. Thus, the preferred short-range ordering among Ni, Al, and Ti may intensify during solidification and serve as the precursors to nucleating the Ni-Al-Ti-rich L2_1 phase. The weak bonding between V and the other elements (Ni, Al, and Ti) may promote the formation of the V-rich BCC phase. The preferred interatomic bonding among Ni, Al, and Ti can also be intuitively observed from the snapshot of the atomic structure at $T = 3000$ K (Fig. 6(b)). The present calculation results of partial PDFs were in line with the above experimental observations, and further verified the design strategy of EHEAs (see Supplementary Materials). Furthermore, the predicted diffusion constants via AIMD simulations through plotting the mean square displacement (MSD) versus time (Fig. 6(c)) reveal that Ti has the lowest diffusivity, followed by Al, and V has the highest diffusivity, followed by Ni (see the upper left inset of Fig. 6(c)). This trend indicates that the relatively-slow diffusion capabilities of Ti and Al and the relatively-quick diffusion capability of V will facilitate the formation of energetically-favorable Ti-Al-Ni and V clusters, respectively, which is consistent with the results of partial PDFs.

The DFT calculations were conducted to understand the phase

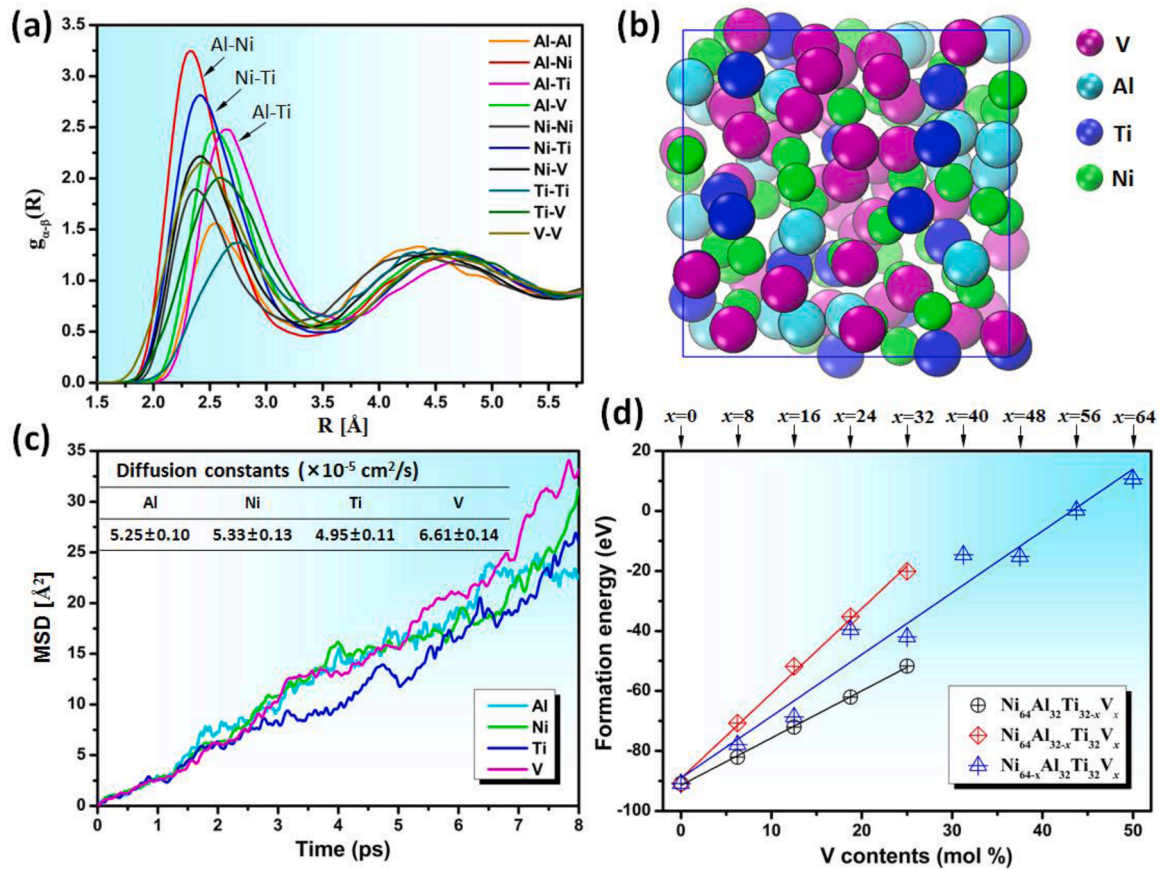


Fig. 6. First-principles calculations on the $\text{Al}_{17}\text{Ni}_{34}\text{Ti}_{17}\text{V}_{32}$ alloy. (a) AIMD-simulated partial PDFs at $T = 3000$ K. (b) A snapshot of the atomic structure during AIMD simulations. (c) The calculated results for MSD versus time of each element, and the inset shows the predicted diffusion constants of various elements at $T = 3000$ K. (d) DFT-predicted energies of formation by substituting V for Ni, Al, and Ti in the Ni_2AlTi -type L_{21} phase.

formation and stability of the present EHEA. To confirm the presence of an energetical preference for the formation of L_{21} and BCC phases, substituting V for Ni, Al, and Ti in the Ni_2AlTi -type L_{21} phase, respectively predicts the energies of formation (E_f) of the various virtual compositions in ternary and quaternary systems via DFT calculations. The results reveal that substituting V for all the three elements causes almost a linear increase of the energy (Fig. 6(d) and Table 3), which indicates that such substitution is energetically unfavorable, and consequently, the V solubility in the L_{21} phase should be limited. This trend is consistent with the present experimental results that the V content in the eutectic L_{21} phase is very low (i.e., 2.29 at% V in the as-cast state), and V is rejected from the L_{21} matrix to form the V-rich BCC precipitates during solidification from high temperatures (see Figs. 2(f), 4(a), and S6(b)). Similarly, the Ni, Al, and Ti elements were rejected from the BCC matrix to form Ni-Al-Ti-rich L_{21} precipitates (see Figs. 2(c), (d), 3(a) and S6(a)). Meanwhile, the DFT calculations also confirm the initial model predictions of EHEA design with L_{21} and BCC structures (see Supplementary Materials).

Phase diagrams can provide the detailed information on the stability of phases as a function of composition, temperature, and pressure. The Ni_2AlTi (L_{21})-V (BCC) pseudo-binary phase diagram in Fig. S3(a) reveals a valley point at $x(\text{V}) = 31.3$ at.% and $T = 1296$ °C, which is close to the

so-called deep eutectic point [70]. The eutectic reaction ($\text{L} \rightarrow \text{L}_{21} + \text{BCC}$) occurs at this point, its solidification finishes in a narrow temperature range, from 1296 to 1200 °C, and then the $\text{L}_{21} + \text{BCC}$ duplex structure is obtained at last. The phase transformation of the present $\text{Al}_{17}\text{Ni}_{34}\text{Ti}_{17}\text{V}_{32}$ EHEA was predicted during solidification (Fig. S3(b)), which indicates that the L_{21} and BCC phases emerged nearly at the same time and kept stable until room temperature, confirming the excellent phase stability of the present experimental observations. In addition, the equilibrium phase volume fractions for L_{21} and BCC phases in the $\text{Al}_{17}\text{Ni}_{34}\text{Ti}_{17}\text{V}_{32}$ EHEA at 800 °C are predicted to be 66.5% and 33.5%, respectively, which is very close to the experimental results annealed at 800 °C for 30 h (i.e., 65.3% L_{21} and 34.7% BCC). The comparison of the experimental data and the results from the phase-diagram calculations indicates that there is a reasonably good agreement between them, and the outstanding thermal stability of the present $\text{Al}_{17}\text{Ni}_{34}\text{Ti}_{17}\text{V}_{32}$ EHEA was further confirmed.

4.2. Strengthening mechanisms

The superior mechanical properties of the $\text{Al}_{17}\text{Ni}_{34}\text{Ti}_{17}\text{V}_{32}$ EHEA, especially at elevated temperatures, should be related to the unique strengthening mechanisms in this alloy. We now discuss the mechanisms

Table 3

DFT-predicted energies of formation (eV) of the various virtual compositions in L_{21} ternary and quaternary systems.

	$x = 0$	$x = 8$	$x = 16$	$x = 24$	$x = 32$	$x = 40$	$x = 48$	$x = 56$	$x = 64$
$\text{Ni}_{64}\text{Al}_{32}\text{Ti}_{32-x}\text{V}_x$	-90.835	-82.097	-72.061	-62.045	-51.738	-	-	-	-
$\text{Ni}_{64}\text{Al}_{32-x}\text{Ti}_{32}\text{V}_x$	-90.835	-70.723	-51.850	-35.225	-20.137	-	-	-	-
$\text{Ni}_{64-x}\text{Al}_{32}\text{Ti}_{32}\text{V}_x$	-90.835	-77.913	-68.657	-39.545	-42.008	-14.647	-15.202	0.242	10.654

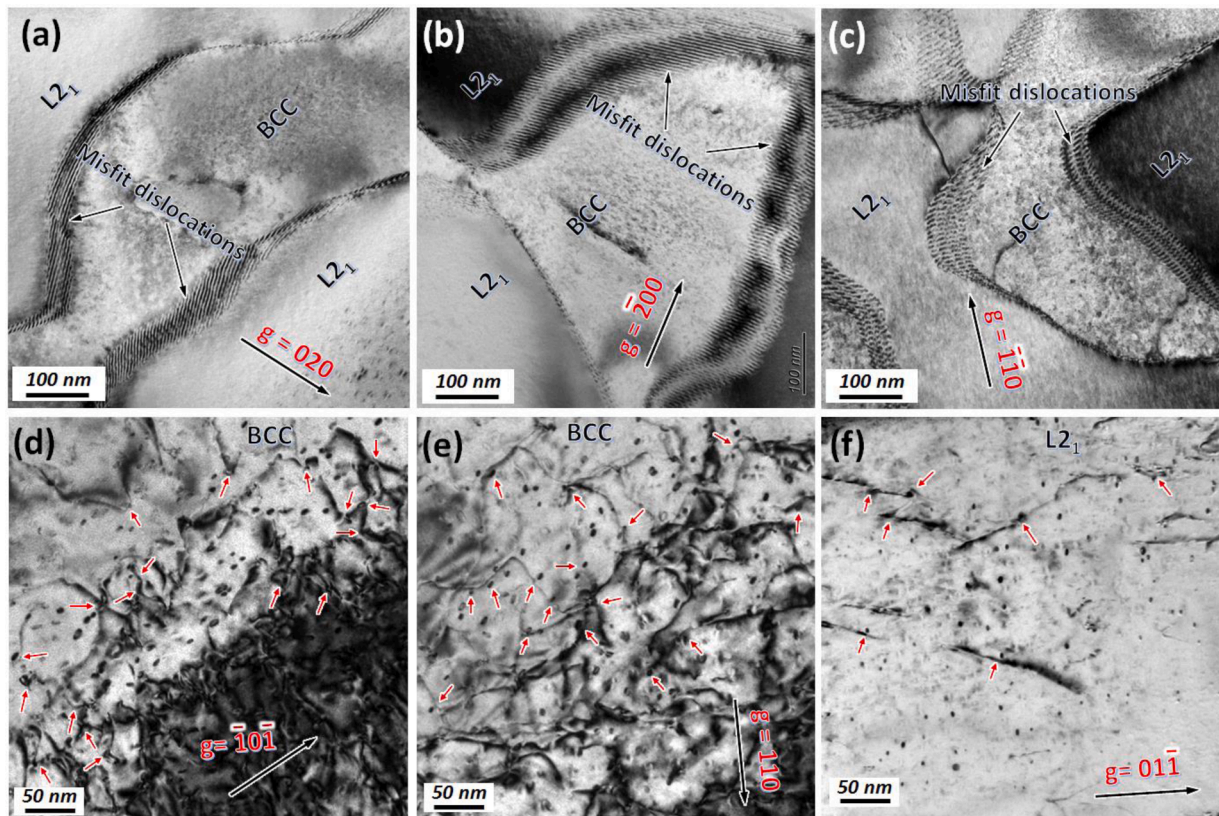


Fig. 7. TEM characterization of the $\text{Al}_{17}\text{Ni}_{34}\text{Ti}_{17}\text{V}_{32}$ alloy. (a–c) Two-beam BF TEM images of the eutectic-phase interface dislocations feature of the as-cast sample with different g vectors. The g vector is annotated in each image with the direction shown by the black arrow. (d–e) Two-beam BF TEM images of a $\approx 10\%$ plastically deformed sample at 800°C with g vectors of $\bar{1}0\bar{1}$ and 110 , respectively, showing the interactions between dislocations and nanoprecipitates within the BCC phase, which are indicated by the red arrows. (f) Two-beam BF TEM images of a $\approx 10\%$ plastically deformed sample at 800°C with g vectors of $01\bar{1}$, showing the interactions between dislocations and nanoprecipitates within the L_{21} phase, which are indicated by the red arrows.

that are involved.

As discussed above, both the experimental results and theoretical simulations substantiate the outstanding phase and microstructural thermal stability of the $\text{Al}_{17}\text{Ni}_{34}\text{Ti}_{17}\text{V}_{32}$ EHEA, which provides guarantee for the retention of high levels of hardness/strength at elevated temperatures.

The Ni–Al–Ti-rich Heusler phase, as one of the eutectic phases in this EHEA system, can be considered as being formed on the base of the NiAl-based B2 phase by Ti doping that gives rise to an additional degree of order and more thermally stable than the B2 phase [71]. In the consideration of the unique L_{21} crystal structure of the Heusler phase, only the $\langle 110 \rangle$ slip is favored since both the $\langle 100 \rangle$ and $\langle 111 \rangle$ slips would involve the creation of a fault [71]. However, the occurrence of cross-slip for $1/2\langle 110 \rangle$ dislocations in this Heusler phase is impossible because the $\langle 110 \rangle$ screw dislocation cannot transfer from one $\{110\}$ plane to another, as planes of this type do not intersect in the $\langle 110 \rangle$ direction [72]. This trend was also corroborated by the hard sphere model [73], which reveals that shear on a cube plane directly along the $\langle 110 \rangle$ direction is extremely impossible in the L_{21} structure. Thus, an inability of cross-slip for $1/2\langle 110 \rangle$ dislocations has eliminated one way by which dislocations may circumvent obstacles during high-temperature deformation [72]. In short, the introduction of the Heusler phase containing a high content of low-density elements (Al and Ti) as one of the eutectic phases could endow the possibility of high strengths, low densities, and excellent thermal stability in EHEAs, which is in line with our initial design goals.

Before mechanical deformation, the preexisting interfacial dislocation networks can be distinctly identified (see Figs. 2(c) and 7(a)–(c)). The lattice mismatch between the eutectic BCC and L_{21} phases is

accommodated by two orthogonal sets of $1/2\langle 100 \rangle$ edge dislocations (Fig. 7(a)–(c)). It is widely known that the predominant slip vector in the disordered BCC structure during room-/high-temperature deformation is $1/2\langle 111 \rangle$ (the closed-packed orientation of the BCC structure) [74, 75]. Thus, great differences in operative glide modes exist between the L_{21} phase ($1/2\langle 110 \rangle$), BCC phase ($1/2\langle 111 \rangle$), and phase interface ($1/2\langle 100 \rangle$), which indicates that the dislocations produced during high-temperature deformation cannot simply glide through the phase interfaces via the cutting mechanism [76]. The two eutectic phases deform through gliding on their respective characteristic slip systems, and the dislocations within each phase interact with the preexisting interfacial dislocation networks and are hindered by them, which significantly decrease the overall dislocation mobility [71].

Additionally, the high density of coherent nanoprecipitates is present in this EHEA, and considerable pinned dislocations can be observed within both the eutectic BCC and L_{21} phases from the deformed samples (Fig. 7(d)–(f)). This feature indicates the strong interactions between dislocations and nanoprecipitates, and thus, the high-temperature mechanical properties of the EHEA can also be enhanced via precipitation strengthening. Precipitation strengthening, as one of the important strengthening mechanisms, has been widely reported in the HEA systems that contain various precipitates [52,77]. Furthermore, a cube-on-cube semi-coherent interface with a low lattice misfit (2.4%) is present between the eutectic L_{21} and BCC phases, which can refine the eutectic microstructure and stabilize the eutectic phases and their interface with a high number density. This trend can further enhance the high-temperature strengths and thermal stability for the present EHEA. Also, the low misfit semi-coherent eutectic phase interface belongs to the strong interfacial combination, which can decrease the cracking

tendency of eutectic phase interface during deformation process. In addition, during solidification and cooling of the lamellar composite from the solidification temperature, the different coefficients of thermal expansion (CTEs) of individual layers result in the difference in thermal deformation. Below a certain temperature as called the joining temperature, the layers become bonded and phase-specific stresses start to develop [78,79]. Such stresses may also contribute to the improvement of mechanical properties of the $\text{Al}_{17}\text{Ni}_{34}\text{Ti}_{17}\text{V}_{32}$ EHEA, which will be estimated in our future work.

5. Conclusions

In summary, we proposed a valid and universal design strategy for the development of lightweight, ultrastrong, and high thermal-stable EHEAs by introducing the low-density-element-contained Heusler-type (L_{21}) phase with a high-degree of order and constructing the low lattice misfit eutectic-phase interface. Based on this new strategy, we successfully designed a novel $\text{Al}_{17}\text{Ni}_{34}\text{Ti}_{17}\text{V}_{32}$ EHEA, with uniform and ultrafine lamellar structures (interlamellar spacing ~ 320 nm) and one of the lowest densities (~ 6.2 g/cm³) among all EHEAs reported previously. This bulk EHEA exhibits exceptional size and microstructural stability, and has much higher high-temperature hardness and SYs than most reported RHEAs, LWHEAs, EHEAs, and conventional superalloys. The AIMD simulations, DFT calculations, and CALPHAD predictions further substantiated the thermal stability of the $\text{Al}_{17}\text{Ni}_{34}\text{Ti}_{17}\text{V}_{32}$ EHEA. The EHEA's superior elevated-temperature properties mainly attributes to the ultrafine and thermal-stable eutectic structures arisen from the low lattice misfit, extremely stable L_{21} structure, and low dislocation mobility originated from the hindrance of preexisting eutectic-phase interfacial dislocation networks and nanoprecipitates.

Overall, the present lightweight EHEA systems composed of L_{21} and BCC structures are a promising candidate for elevated-temperature applications suffering from compressive loading.

Declaration of Competing Interest

The authors declare that they have no known competing financial interests or personal relationships that could have appeared to influence the work reported in this paper.

Acknowledgments

This work was supported by the National Natural Science Foundation of China (Nos. 52001051 and U20A20278), the Project funded by China Postdoctoral Science Foundation (2021T140082), the National Key Research and Development Program of China (Nos. 2018YFA0702901 and 2019YFA0209901), Liao Ning Revitalization Talents Program (No. XLYC1807047), Major special project of "scientific and technological innovation 2025" in Ningbo (No. 2019B10086). P. K. Liaw appreciates support from the National Science Foundation (DMR1611180 and 1809640) and the US Army Research Office (W911NF13-1-0438 and W911NF-19-2-0049).

Supplementary materials

Supplementary material associated with this article can be found, in the online version, at [doi:10.1016/j.actamat.2023.118806](https://doi.org/10.1016/j.actamat.2023.118806).

References

- [1] A. Devaraj, V.V. Joshi, A. Srivastava, S. Manandhar, V. Moxson, V.A. Duz, C. Lavender, A low-cost hierarchical nanostructured beta-titanium alloy with high strength, *Nat. Commun.* 7 (2016) 11176.
- [2] X. Zhang, Y. Chen, J. Hu, Recent advances in the development of aerospace materials, *Prog. Aerosp. Sci.* 97 (2018) 22–34.
- [3] R.C. Reed, *The Superalloys: Fundamentals and Applications*, Cambridge University Press, 2008.
- [4] R. Feng, M.C. Gao, C. Zhang, W. Guo, J.D. Poplawsky, F. Zhang, J.A. Hawk, J. C. Neuefeind, Y. Ren, P.K. Liaw, Phase stability and transformation in a light-weight high-entropy alloy, *Acta Mater.* 146 (2018) 280–293.
- [5] Z. Sun, C.H. Liebscher, S. Huang, Z. Teng, G. Song, G. Wang, M. Asta, M. Rawlings, M.E. Fine, P.K. Liaw, New design aspects of creep-resistant NiAl-strengthened ferritic alloys, *Scr. Mater.* 68 (2013) 384–388.
- [6] N.Q. Vo, C.H. Liebscher, M.J.S. Rawlings, M. Asta, D.C. Dunand, Creep properties and microstructure of a precipitation-strengthened ferritic Fe-Al-Ni-Cr alloy, *Acta Mater.* 71 (2014) 89–99.
- [7] Y.P. Lu, Y. Dong, S. Guo, L. Jiang, H.J. Kang, T.M. Wang, B. Wen, Z.J. Wang, J. C. Jie, Z.Q. Cao, H.H. Ruan, T.J. Li, A promising new class of high-temperature alloys: eutectic high-entropy alloys, *Sci. Rep.* 4 (2014) 6200.
- [8] Y.P. Lu, Y. Dong, H. Jiang, Z.J. Wang, Z.Q. Cao, S. Guo, T.M. Wang, T.J. Li, P. K. Liaw, Promising properties and future trend of eutectic high entropy alloys, *Scr. Mater.* 187 (2020) 202–209.
- [9] B. Cantor, I.T.H. Chang, P. Knight, A.J.B. Vincent, Microstructural development in equiatomic multicomponent alloys, *Mater. Sci. Eng. A* 375–377 (2004) 213–218.
- [10] J.W. Yeh, S.K. Chen, S.J. Lin, J.Y. Gan, T.S. Chin, T.T. Shun, C.H. Tsau, S.Y. Chang, Nanostructured high-entropy alloys with multiple principal elements: novel alloy design concepts and outcomes, *Adv. Eng. Mater.* 6 (2004) 299–303.
- [11] C.S. Tiwary, P. Pandey, S. Sarkar, R. Das, S. Samal, K. Biswas, K. Chattopadhyay, Five decades of research on the development of eutectic as engineering materials, *Prog. Mater. Sci.* 123 (2022), 100793.
- [12] I.S. Wani, T. Bhattacharjee, S. Sheikh, Y.P. Lu, S. Chatterjee, P.P. Bhattacharjee, S. Guo, N. Tsuji, Ultrafine-grained AlCoCrFeNi_{2.1} eutectic high-entropy alloy, *Mater. Res. Lett.* 4 (2016) 174–179.
- [13] P. Shi, W. Ren, T. Zheng, Z. Ren, X. Hou, J. Peng, P. Hu, Y. Gao, Y. Zhong, P. K. Liaw, Enhanced strength–ductility synergy in ultrafine-grained eutectic high-entropy alloys by inheriting microstructural lamellae, *Nat. Commun.* 10 (2019) 489.
- [14] T. Xiong, S. Zheng, J. Pang, X. Ma, High-strength and high-ductility AlCoCrFeNi_{2.1} eutectic high-entropy alloy achieved via precipitation strengthening in a heterogeneous structure, *Scr. Mater.* 186 (2020) 336–340.
- [15] J. Miao, H. Liang, A. Zhang, J. He, J. Meng, Y. Lu, Tribological behavior of an AlCoCrFeNi_{2.1} eutectic high entropy alloy sliding against different counterfaces, *Tribol. Int.* 153 (2021), 106599.
- [16] P. Shi, R. Li, Y. Li, Y. Wen, Y. Zhong, W. Ren, Z. Shen, T. Zheng, J. Peng, X. Liang, P. Hu, N. Min, Y. Zhang, Y. Ren, P.K. Liaw, D. Raabe, Y. Wang, Hierarchical crack buffering triples ductility in eutectic herringbone high-entropy alloys, *Science* 373 (2021) 912–918.
- [17] P. Shi, Y. Zhong, Y. Li, W. Ren, T. Zheng, Z. Shen, B. Yang, J. Peng, P. Hu, Y. Zhang, P.K. Liaw, Y. Zhu, Multistage work hardening assisted by multi-type twinning in ultrafine-grained heterostructural eutectic high-entropy alloys, *Mater. Today* 41 (2020) 62–71.
- [18] X. Jin, J. Bi, L. Zhang, Y. Zhou, X.Y. Du, Y.X. Liang, B.S. Li, A new CrFeNi₂Al eutectic high entropy alloy system with excellent mechanical properties, *J. Alloy. Compd.* 770 (2019) 655–661.
- [19] Q.F. Wu, Z.J. Wang, T. Zheng, D. Chen, Z.S. Yang, J.J. Li, J.J. Kai, J.C. Wang, A casting eutectic high entropy alloy with superior strength-ductility combination, *Mater. Lett.* 253 (2019) 268–271.
- [20] D. Liu, P. Yu, G. Li, P.K. Liaw, R. Liu, High-temperature high-entropy alloys AlxCo15Cr15Ni70-x based on the Al-Ni binary system, *Mater. Sci. Eng. A* 724 (2018) 283–288.
- [21] I. Baker, F.L. Meng, M. Wu, A. Brandenberg, Recrystallization of a novel two-phase FeNiMnAlCr high entropy alloy, *J. Alloy. Compd.* 656 (2016) 458–464.
- [22] X. Jin, Y. Zhou, L. Zhang, X.Y. Du, B.S. Li, A new pseudo binary strategy to design eutectic high entropy alloys using mixing enthalpy and valence electron concentration, *Mater. Des.* 143 (2018) 49–55.
- [23] M. Wu, S. Wang, H. Huang, D. Shu, B. Sun, CALPHAD aided eutectic high-entropy alloy design, *Mater. Lett.* 262 (2020), 127175.
- [24] H. Jiang, D. Qiao, Y. Lu, Z. Ren, Z. Cao, T. Wang, T. Li, Direct solidification of bulk ultrafine-microstructure eutectic high-entropy alloys with outstanding thermal stability, *Scr. Mater.* 165 (2019) 145–149.
- [25] Y. Tan, J. Li, J. Wang, M. Kolbe, H. Kou, Microstructure characterization of CoCrFeNiMnPd_x eutectic high-entropy alloys, *J. Alloy. Compd.* 731 (2018) 600–611.
- [26] M.R. Rahul, G. Phanikumar, Design of a seven-component eutectic high-entropy alloy, *Metall. Mater. Trans. A* 50A (2019) 2594–2598.
- [27] L. Jiang, Z.Q. Cao, J.C. Jie, J.J. Zhang, Y.P. Lu, T.M. Wang, T.J. Li, Effect of Mo and Ni elements on microstructure evolution and mechanical properties of the CoFeNi_xV_{1-x} high entropy alloys, *J. Alloy. Compd.* 649 (2015) 585–590.
- [28] H. Jiang, H.Z. Zhang, T.D. Huang, Y.P. Lu, T.M. Wang, T.J. Li, Microstructures and mechanical properties of Co₂MoxNi₂VW_x eutectic high entropy alloys, *Mater. Des.* 109 (2016) 539–546.
- [29] Y.P. Lu, H. Jiang, S. Guo, T.M. Wang, Z.Q. Cao, T.J. Li, A new strategy to design eutectic high-entropy alloys using mixing enthalpy, *Intermetallics* 91 (2017) 124–128.
- [30] H. Jiang, K. Han, X. Gao, Y. Lu, Z. Cao, M.C. Gao, J.A. Hawk, T. Li, A new strategy to design eutectic high-entropy alloys using simple mixture method, *Mater. Des.* 142 (2018) 101–105.
- [31] X. Lin, M. Wang, G. Ren, D. Qiao, Y. Lu, T. Wang, T. Li, Microstructure evolution and mechanical properties of CrFeNi_xV_{0.64}Ta_{0.36} eutectic high-entropy alloys, *Mater. Charact.* 181 (2021), 111449.
- [32] F. Stein, M. Palm, G. Sauthoff, Structure and stability of Laves phases part II—Structure type variations in binary and ternary systems, *Intermetallics* 13 (2005) 1056–1074.

- [33] M. Wang, Y. Lu, T. Wang, C. Zhang, Z. Cao, T. Li, P.K. Liaw, A novel bulk eutectic high-entropy alloy with outstanding as-cast specific yield strengths at elevated temperatures, *Scr. Mater.* 204 (2021), 114132.
- [34] J.F. Radavich, Long time stability of a wrought alloy 718 disk, superalloy 718, *Metall. Appl.* (1989) 257–268.
- [35] Y.J. Chang, A.C. Yeh, The evolution of microstructures and high temperature properties of $\text{AlxCo}_{1.5}\text{CrFeNi}_{1.5}\text{Tiy}$ high entropy alloys, *J. Alloy. Compd.* 653 (2015) 379–385.
- [36] X.D. Lu, J.H. Du, Q. Deng, High temperature structure stability of GH4169 superalloy, *Mater. Sci. Eng. A* 559 (2013) 623–628.
- [37] J. Liu, J. Cao, X. Lin, X. Song, J. Feng, Microstructure and mechanical properties of diffusion bonded single crystal to polycrystalline Ni-based superalloys joint, *Mater. Des.* 49 (2013) 622–626.
- [38] D. Hu, J. Mao, J. Song, F. Meng, X. Shan, R. Wang, Experimental investigation of grain size effect on fatigue crack growth rate in turbine disc superalloy GH4169 under different temperatures, *Mater. Sci. Eng. A* 669 (2016) 318–331.
- [39] A.C. Larson, R.B. Von Dreele, General structure analysis system “GSAS”, Los Alamos National Laboratory Report LAUR 86-748, 1994.
- [40] L.B. McCusker, R.B. Von Dreele, D.E. Cox, D. Louer, P. Scardi, Rietveld refinement guidelines, *J. Appl. Cryst.* 32 (1999) 36–50.
- [41] L. Finger, D. Cox, A. Jephcoat, A correction for powder diffraction peak asymmetry due to axial divergence, *J. Appl. Crystallogr.* 27 (1994) 892–900.
- [42] P.W. Stephens, Phenomenological model of anisotropic peak broadening in powder diffraction, *J. Appl. Crystallogr.* 32 (1999) 281–289.
- [43] Pandat™, Thermodynamic Calculations and Kinetic Simulations, CompuTherm LLC, 2021.
- [44] J. Hutter, M. Iannuzzi, F. Schiffmann, J. VandeVondele, CP2K: atomistic simulations of condensed matter systems, *Comput. Mol. Sci.* 4 (2014) 15–25.
- [45] J.P. Perdew, K. Burke, M. Ernzerhof, Generalized gradient approximation made simple, *Phys. Rev. Lett.* 77 (1996) 3865–3868.
- [46] S. Grimme, Semiempirical GGA-type density functional constructed with a long-range dispersion correction, *J. Comput. Chem.* 27 (2006) 1787–1799.
- [47] J. VandeVondele, J. Hutter, Gaussian basis sets for accurate calculations on molecular systems in gas and condensed phases, *J. Chem. Phys.* 127 (2007), 114105.
- [48] J. VandeVondele, M. Krack, F. Mohamed, M. Parrinello, T. Chassaing, J. Hutter, QUICKSTEP: fast and accurate density functional calculations using a mixed Gaussian and plane waves approach, *Comput. Phys. Commun.* 167 (2005) 103–128.
- [49] S. Goedecker, M. Teter, J. Hutter, Separable dual-space Gaussian pseudopotentials, *Phys. Rev. B* 54 (1996) 1703–1710.
- [50] C. Hartwigsen, S. Goedecker, J. Hutter, Relativistic separable dual-space Gaussian pseudopotentials from H to Rn, *Phys. Rev. B* 58 (1998) 3641–3662.
- [51] G. Bussi, D. Donadio, M. Parrinello, Canonical sampling through velocity rescaling, *J. Chem. Phys.* 126 (2007), 014101.
- [52] L.Y. Liu, Y. Zhang, J.H. Han, X.Y. Wang, W.Q. Jiang, C.T. Liu, Z.W. Zhang, P. K. Liaw, Nano-precipitate-strengthened high entropy alloys, *Adv. Sci.* 8 (2021), 2100870.
- [53] E.P. George, D. Raabe, R.O. Ritchie, High-entropy alloys, *Nat. Rev. Mater.* 4 (2019) 515–534.
- [54] D.B. Miracle, O.N. Senkov, A critical review of high entropy alloys and related concepts, *Acta Mater.* 122 (2017) 448–511.
- [55] T.K. Tsao, A.C. Yeh, C.M. Kuo, H. Murakami, On the superior high temperature hardness of precipitation strengthened high entropy Ni-based alloys: high entropy Ni-based alloys, *Adv. Eng. Mater.* 19 (2016), 1600475.
- [56] C.J. Tong, M.R. Chen, J.W. Yeh, S.J. Lin, S.K. Chen, T.T. Shun, S.Y. Chang, Mechanical performance of the AlxCoCrCuFeNi high-entropy alloy system with multiprincipal elements, *Metall. Mater. Trans. A* 36 (2005) 1263–1271.
- [57] Y. Zhou, X. Jin, L. Zhang, X. Du, B. Li, A hierarchical nanostructured $\text{Fe}_{34}\text{Cr}_{34}\text{Ni}_{14}\text{Al}_{14}\text{Co}_4$ high-entropy alloy with good compressive mechanical properties, *Mater. Sci. Eng. A* 716 (2018) 235–239.
- [58] D.G. Shaysultanov, G.A. Salishchev, Y.V. Ivanisenko, S.V. Zherebtsov, M. A. Tikhonovsky, N.D. Stepanov, Novel $\text{Fe}_{36}\text{Mn}_{21}\text{Cr}_{18}\text{Ni}_{15}\text{Al}_{10}$ high entropy alloy with bcc/B2 dual-phase structure, *J. Alloy. Compd.* 705 (2017) 756–763.
- [59] R. Feng, C. Zhang, M.C. Gao, Z. Pei, F. Zhang, Y. Chen, D. Ma, K. An, J. D. Poplawsky, L. Ouyang, Y. Ren, J.A. Hawk, M. Widom, P.K. Liaw, High-throughput design of high-performance lightweight high-entropy alloys, *Nat. Commun.* 12 (2021) 4329.
- [60] O.N. Senkov, G.B. Wilks, J.M. Scott, D.B. Miracle, Mechanical properties of $\text{Nb}_{25}\text{Mo}_{25}\text{Ta}_{25}\text{W}_{25}$ and $\text{V}_{20}\text{Nb}_{20}\text{Mo}_{20}\text{Ta}_{20}\text{W}_{20}$ refractory high entropy alloys, *Intermetallics* 19 (2011) 698–706.
- [61] C. Lee, G. Song, M.C. Gao, R. Feng, P. Chen, J. Brechtel, Y. Chen, K. An, W. Guo, J. D. Poplawsky, S. Li, A.T. Samaei, W. Chen, A. Hu, H. Choo, P.K. Liaw, Lattice distortion in a strong and ductile refractory high-entropy alloy, *Acta Mater.* 160 (2018) 158–172.
- [62] O.N. Senkov, J.M. Scott, S.V. Senkova, F. Meisenkothen, D.B. Miracle, C. F. Woodward, Microstructure and elevated temperature properties of a refractory TaNbHfZrTi alloy, *J. Mater. Sci.* 47 (2012) 4062–4074.
- [63] N.D. Stepanov, N.Y. Yurchenko, E.S. Panina, M.A. Tikhonovsky, S.V. Zherebtsov, Precipitation-strengthened refractory $\text{Al}_{0.5}\text{CrNbTi}_2\text{V}_{0.5}$ high entropy alloy, *Mater. Lett.* 188 (2017) 162–164.
- [64] N.D. Stepanov, N.Y. Yurchenko, D.V. Skibin, M.A. Tikhonovsky, G.A. Salishchev, Structure and mechanical properties of the AlCrNbTiV ($x = 0, 0.5, 1, 1.5$) high entropy alloys, *J. Alloy. Compd.* 652 (2015) 266–280.
- [65] O.N. Senkov, S.V. Senkova, D.B. Miracle, C. Woodward, Mechanical properties of low-density, refractory multi-principal element alloys of the Cr–Nb–Ti–V–Zr system, *Mater. Sci. Eng. A* 565 (2013) 51–62.
- [66] S. Zherebtsov, G. Salishchev, R. Galeyev, K. Maekawa, Mechanical properties of Ti–6Al–4V titanium alloy with submicrocrystalline structure produced by severe plastic deformation, *Mater. Trans.* 46 (2005) 2020–2025.
- [67] C. Stallybrass, G. Sauthoff, Ferritic Fe–Al–Ni–Cr alloys with coherent precipitates for high-temperature applications, *Mater. Sci. Eng. A* 387–389 (2004) 985–990.
- [68] D. Caillard, J. L. Martin, Thermally Activated Mechanisms in Crystal Plasticity, Elsevier, Oxford, 2003.
- [69] L.J. Santodonato, Y. Zhang, M. Feygensohn, C.M. Parish, M.C. Gao, M.K. Miller, R.J. K. Weber, J.C. Neuefeind, Z. Tang, P.K. Liaw, Deviation from high-entropy configurations in the atomic distributions of a multi-principal-element alloy, *Nat. Commun.* 6 (2014) 5964–5971.
- [70] C. Zhang, F. Zhang, S.L. Chen, W.S. Cao, Computational thermodynamics aided high-entropy alloy design, *JOM* 64 (2012) 839–845.
- [71] R.S. Polvani, W.S. Tzeng, P.R. Strutt, High temperature creep in a semi-coherent $\text{NiAl-Ni}_2\text{AlTi}$ alloy, *Metall. Trans. A* 7 (1976) 33–40.
- [72] P.R. Strutt, R.S. Polvani, J.C. Ingram, Creep behavior of the heusler type structure alloy Ni_2AlTi , *Metall. Mater. Trans. A* 7 (1976) 23–31.
- [73] E.P. Lautenschlager, T. Hughes, J.O. Brittain, Slip in hard-sphere CsCl Lmodels, *Acta Metall.* 15 (1967) 1347–1357.
- [74] R. Feng, B. Feng, M.C. Gao, C. Zhang, J.C. Neuefeind, J.D. Poplawsky, Y. Ren, K. An, M. Widom, P.K. Liaw, Superior high-temperature strength in a supersaturated refractory high-entropy alloy, *Adv. Mater.* 33 (2021), 2102401.
- [75] F. Wang, G.H. Balbus, S. Xu, Y. Su, J. Shin, P.F. Rottmann, K.E. Knippling, J. C. Stinville, L.H. Mills, O.N. Senkov, I.J. Beyerlein, T.M. Pollock, D.S. Gianola, Multiplicity of dislocation pathways in a refractory multiprincipal element alloy, *Science* 370 (2020) 95–101.
- [76] S.M. Copley, B.H. Kear, Temperature and orientation dependence of the flow stress in off-stoichiometric Ni sub 3 Al/gamma' phase/(Strength characteristics of single crystals of nickel aluminide/gamma phase/, discussing temperature and orientation dependence of work hardening, *Trans. TMS AIME* 239 (1967) 977.
- [77] Y.J. Liang, L. Wang, Y. Wen, B. Cheng, Q. Wu, T. Cao, Q. Xiao, Y. Xue, G. Sha, Y. Wang, Y. Ren, X. Li, L. Wang, F. Wang, H. Cai, High-content ductile coherent nanoprecipitates achieve ultrastrong high-entropy alloys, *Nat. Commun.* 9 (2018) 4063.
- [78] D. Yu, K. An, X. Chen, H. Bei, Phase-specific deformation behavior of a NiAl-Cr(Mo) lamellar composite under thermal and mechanical loads, *J. Alloy. Compd.* 656 (2016) 481–490.
- [79] T. Chartier, D. Merle, J.L. Besson, Laminar ceramic composites, *J. Eur. Ceram. Soc.* 15 (1995) 101–107.